Facile preparation with high yield of a 3D porous graphitic carbon nitride for dramatically enhanced photocatalytic H_2 evolution under visible light

Bing Luo, Rui Song, Jiafeng Geng, Dengwei Jing*, Yazhou Zhang

International Research Center for Renewable Energy & State Key Laboratory of Multiphase Flow in Power Engineering, Xi'an Jiaotong University, Xi'an, 710049, China

A B S T R A C T

For its performance enhancement, graphitic carbon nitride (CN) has been prepared by acid protonation or heat etching methods, both with quite low product yield. In the present work, three dimension porous CN was prepared in a facile way with high yield by both operation of acid protonation and thermal oxidation. It was found that the CN subjected to firstly acid protonation and secondly heat etching (CN-HT) exhibited almost 29.5 times higher H_2 evolution rate compared to the pristine CN. While the sample subjecting to a reverse operation sequence only had 7.3 times improvement. Compared to the re-calcined sample without protonation, it was found that the introduction of protons (H^+) into CN structure before re-calcination significantly enhanced its activity for visible light driven photocatalytic H_2 generation. After full characterizations, the significantly enhanced activity was attributed to the greatly enlarged surface areas, the promoted charge carriers separation and immigration efficiency, the improved reduction potential of photo-induced electrons, as well as the strengthened hydrophilic interface. Our study is expected to provide a new facile approach for tailoring the microstructure of layered materials to achieve improved performance not only for the application of photocatalysis, but also in many other fields.

1. Introduction

Photocatalytic water splitting to generate hydrogen and oxygen is one of the promising sustainable approaches to solve the energy and environment crisis [1,2]. Generally, the microscopic photocatalytic water splitting processes contain three primary steps [1,2]: (1) the absorption of photos via semiconductor excitons excitation to generate electron/hole pairs; (2) the separation, transportation, and recombination of photo-induced charge carriers; (3) the photocatalytic redox reactions with the reactive radicals on the semiconductor surface. For a specified photocatalyst, the modification of last two steps is the most effective method to improve its catalytic ability.

Graphitic carbon nitride (g-C_3N_4) is a promising material with unique two-dimensional structure. It can be seen as a nitrogen substituted graphene-like layered material, wherein tri-s-triazine units are bonded by amino groups within intralayer and weak van der Waals forces between layers. The intrinsic visible light response feature, suitable electronic structure for water splitting, green, costless and other advantages further strengthen the potential application of the material in energy conversion field [3–5]. Despite of so many exciting merits, g-C_3N_4 also suffers from several severely disadvantages originating from the incomplete polymerization of the precursors containing amine

groups [6]. For instance, its low specific surface area offers the limited reaction sites, and the high recombination rate of photoinduced charge carriers restricts the redox reaction rate. In order to overcome these disadvantages, tremendous studies have been carried out to develop strategies to promote its photocatalytic performance, such as by designing novel nanostructures [7–9], tuning electronic properties [10,11], doping with heteroatoms [12–14], and constructing heterojunctions [15–17], etc.

Among them, modulating the intrinsic properties of graphitic carbon nitride without introducing other heterocompositions has been proved to be an effective strategy for modifying the electronic structure to obtain fascinating photocatalytic performance [18]. The self-modification approaches, such as thermal oxidation and acid protonation have also been employed to tune the properties of g-C_3N_4 according to the practical demands in different research field [3]. Specially, due to the weak van der Waals force between interlayers, thermal oxidation treatment was found to be able to exfoliate the bulk g-C_3N_4 into fewer layers or nanosheets and even etch the nanolayers into porous nanosheets, which provide much more reaction sites and show great superiority in photogenerated charge carrier transfer and separation due to the shorted moving length to the surface for charge carriers. For instance, Cheng and co-workers reported direct thermal oxidation

exfoliation process of bulk g-C_3N_4 into nanosheets, leading to more superior photocatalytic activities than its bulk g-C_3N_4 counterpart [19]. Xing et al. reported macroscopic foam-like holey ultrathin g-C_3N_4 nanosheets for drastic improvement of visible-light photocatalytic activity by long-time thermal oxidation [20]. In addition, selectively breaking hydrogen bonds, existing in the C–N covalent bonds-dominated intralayer framework of layered carbon nitride, via adjusting thermal oxidation temperature further enhanced photocatalytic hydrogen generation activity under visible light [6].

Regarding to acid protonation on g-C_3N_4, because of the existence of plenty of (-C–N-) motifs in the framework, protons cleave bulk g-C_3N_4 into small pieces and protonate the layers at the same time [21–23]. The protonated bulk g-C_3N_4 with smaller size not only induces electrostatic repulsion, provides better dispersion and a larger specific surface area, but also enables the adjustment of electronic band gaps and a higher ionic conductivity [24,25]. In particular, Zhu et al. prepared single atomic layer g-C_3N_4 nanosheets by intercalating H_2SO_4 into interplanar space to induce the exfoliation of g-C_3N_4 nanosheets for photocatalytic H_2 evolution application [26]. On the other hand, protonated g-C_3N_4 nanosheets are also good candidates for fabricating functional composites due to its tunable surface charge properties by the protons [27,28].

Although the thermal oxidized or acid protonated g-C_3N_4 owns great potential application in catalysis, both of them still suffer from the low product yield [26,29], which may restrict their practical application. On the other hand, to the best of our knowledge, the combination of these two approaches to modify g-C_3N_4 has not been attempted. Therefore, it is of great interest to explore the possible influence of their combined action on g-C_3N_4 for better photocatalytic H_2 evolution performance.

In this work, combined acid protonation and thermal oxidation treatments were carried out on bulk g-C_3N_4, which resulted in three dimension sponge like product with significantly enhanced photocatalytic H_2 evolution performance and also the highly product yield. Interestingly, the operation sequence of the two treating methods has obviously distinct effect on the final H_2 production. The resultant materials were subjected to full characterization for the understanding of the underlying mechanism for the significantly promoted performance of the materials.

2. Experimental section

2.1. Chemicals

All the chemicals, including melamine, hydrochloric acid (37 wt%) were of analytical grade and obtained from Sinopharm Chemical Reagent Co., Ltd. and used without further purification.

2.2. The synthesis of CN

In a typical pristine CN preparation process, 10 g melamine was added into an alumina crucible and heated to 550 °C with a rate of 5 °C min^{-1} and kept at this temperature for another 4 h in air. After cooling to room temperature, the yellow block was grinded into powder.

2.3. Protonating of CN

1 g pristine CN was dispersed into the 20 mL 3 M H^+ solution and kept stirring for 12 h at room temperature. Then, the protonated CN was washed till the supernatant as neutral by the deionized water and dried at 80 °C under vacuum for 12 h. This sample was labeled as CN-H.

2.4. Calcination of pristine CN and the protonated CN

0.2 g pristine CN or the CN-H was added into an alumina crucible

with a cover and heated to an expected temperature (475, 500, 525, 550, 575, and 600 °C) with 5 °C min^{-1} increasing temperature rate and kept at this temperature for 2 h. The sample was named as CN-T and CN-HT, respectively. In addition, the CN-T after HCl treated was labeled as CN-TH. In addition, another two protonation treatments were carried out with same H^+ concentration of the HNO_3 and H_2SO_4 solution. And the corresponding protonated samples were thermal treated at 500 °C only.

2.5. Material characterizations

Powder X-ray diffraction (XRD) patterns were detected to analyze the crystallographic structure and chemical composition of the prepared photocatalyts at room temperature by a PANalytical X'pert MPD Pro diffractometer operated at 40 kV and 40 mA using Ni-filtered Cu-Kα irradiation (Wavelength: 1.5406 Å). Zeta potentials were measured in the pure water of different samples by Zetasizer Nano from Malvern. An FEI Tecnai G2 F30 transmission electron microscope (TEM) at an accelerating voltage of 300 kV was used to characterize the morphology and structure of photocatalysts. Brunauer-Emmette-Teller (BET) measurement was recorded by an accelerated surface area and porosimetry analyzer (Micromeritics ASAP 2020, USA) with N_2 adsorption analysis. Fourier transform infrared spectra (FTIR) were recorded using a Bruker Vertex 70 FTIR spectrophotometer. X-ray photoelectron spectroscopy (XPS) data were obtained on a Kratos Axis-Ultra DLD instrument with a monochromatized Al Kα line source (150 W). All binding energies were referenced to the C 1 s peak at 284.8 eV. UV–vis diffuse reflectance spectra were tested by a HITACHI U4100 instrument equipped with a labsphere diffuse reflectance accessory. Photoluminescence spectra (PL) were measured at room temperature on a PTI QM-4 fluorescence spectrophotometer. Electron paramagnetic resonance (EPR) experiments were performed on a Bruker EMX X-band spectrometer and microwave frequency = 9.40 GHz at room temperature.

2.6. Photoelectrochemical measurements

Photoelectrochemical properties of photocatalysts were measured in a three-electrode cell with a Pt plate as a counter electrode, Ag/AgCl as a reference electrode and an FTO glass loaded with the catalyst as working electrode. Na_2SO_4 (0.5 M, pH = 6.8) aqueous solution was applied as the electrolyte. The transient photocurrent densities were recorded with an applied voltage of 0.4 V vs Ag/AgCl. The working electrode was prepared as follow. The mixture suspension including corresponding photocatalyst powders (1 mg), deionized water (250 μL), ethanol (250 μL) and Nafion solutions (10 μL, DuPont D1020, 10 wt%) was sonicated for 30 min for a well dispersed suspension. The obtained dispersion mixture (100 μL) was dropped on the FTO glass (1.5 × 1.5 cm^2) uniformly, and then naturally dried at room temperature overnight.

2.7. Evaluation of photocatalytic hydrogen production

The photocatalytic hydrogen production ability of different catalysts was evaluated in a gas tight system with a 115 mL side-irradiation Pyrex cell as the photoreactor. A 300 W Xenon lamp was equipped as the simulated light source, and the UV part of the irradiated light was removed by a 420 nm cut-off filter. The gas was sampled with a syringe and quantitatively analyzed on a thermal conductivity detector (TCD) gas chromatograph (NaX zeolite column, Ar as a carrier gas) every 30 min. In a typical photocatalytic hydrogen evolution experiment, 20 mg photocatalyst powder was dispersed into 80 mL aqueous solution containing 10 vol% triethanolamine (TEOA) as a sacrificial reagent. Cocatalyst Pt (1 wt%) was photodeposited in situ on the photocatalysts from the precursor of $H_2PtCl_6 \cdot 6H_2O$. The aqueous suspension was bubbled with N_2 for 20 min to remove dissolved oxygen completely before the photocatalytic reaction. The reaction was carried out at room

temperature.

The apparent quantum efficiency for the hydrogen production of photocatalyst was measured under irradiation of the 300 W Xe lamp with a band-pass filter (420 ± 5 nm). In addition, the intensity of ir-radiated light was detected by a spectrodiometer (Avantes AvaSpec-2048-USB2, Netherlands). The calculation of apparent quantum yield (AQY) was based on the following equation [30]:

$$AQY\,(\%) = \frac{\text{number of reacted electrons}}{\text{number of incident photons}} \times 100\%$$

$$= \frac{2 \times \text{number of evolved} H_2 \text{molecues}}{\text{number of incident photons}} \times 100\%$$

3. Results and discussion

3.1. Photocatalytic H$_2$ evolution activity

Thermal oxidation of pristine CN by re-calcining under high tem-perature results in porous or exfoliated low layer carbon nitrides with fascinating photocatalytic water reduction ability, and also quite low product yield. It has no more than ~30% product yield for the pre-viously reported samples prepared by thermal exfoliation method, as shown in the Table. S1. As a result, to obtain a CN with excellent photocatalytic performance just by annealing approach inevitably leads to a low product yield. In our case, modified CN simultaneously pos-sessing exciting photocatalytic activity and high yield was easily pre-pared by introducing a protonation process before re-calcination. As

shown in the Fig. 1a and b, CN-T (temperature in the range of 475 °C–600 °C) undergos an improvement of photocatalytic H$_2$ evolu-tion rate with the increasing re-calcination temperature, accompanying with decreasing product yield. Obviously, CN-T-600 has the highest H$_2$ evolution reaction (HER) rate and the lowest product yield. However, after introducing protonation before re-calcination, the sample calcined under 500 °C (CN-HT-500) obtains excellent HER performance similar to that of sample CN-T-600 without protonation. But the decreased temperature makes it possible to retain product yield as high as ~62.5%. While it is only 32.3% product yield for CN-T-600. The sig-nificantly enhanced product yield is obviously valuable for the practical application. Therefore, the following discussion about CN-HT will be focused on the sample treated under 500 °C due to its good photo-catalytic performance and the high product yield.

Subsequently, in order to unveil the influence of protonation and thermal oxidation treatment on the photocatalytic H$_2$ production, all the prepared carbon nitrides were evaluated under visible light, cor-responding results demonstrated in the Fig. 1c and Fig. S1. As seen all the samples have a linear increase of H$_2$ production versus time and varied improvements in HER compared to that of pristine CN, 0.076 mmol h^{-1} g^{-1}. Thereinto, CN-H and CN-T achieve a H$_2$ pro-duction rate of 0.23 and 0.62 mmol h^{-1} g^{-1}, respectively. It indicates that both of the protonation and thermal oxidation have a positive ef-fect on boosting H$_2$ evolution. While under the combined action of protonation and thermal oxidation, the operation sequence does sig-nificantly affect the final HER activity. CN-HT has the highest H$_2$ evo-lution rate as high as 2.24 mmol h^{-1} g^{-1}, corresponding to apparent quantum yield of 12.2%. The rate is 29.5 times higher than that of
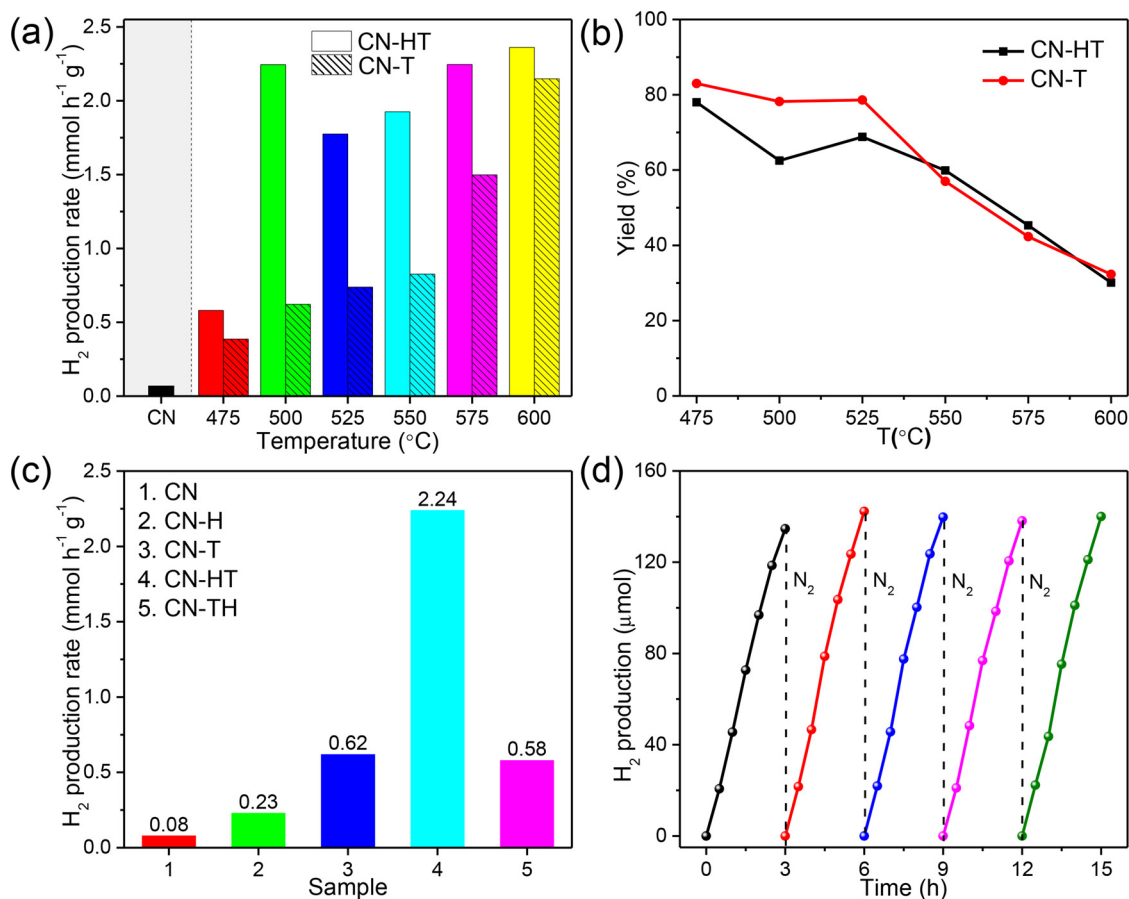

Fig. 1. (a) The dependence of average H$_2$ evolution rate of pristine CN and protonated CN after being treated with different thermal oxidation temperature; (b) The final product yield of CN-T and CN-HT versus temperature; (c) The average H$_2$ evolution rate of pristine CN and modified CN; (d) The stability test of CN-HT within 15 h containing 5 successive cycles. (Reaction conditions: 80 mL aqueous solution containing 10 vol% TEOA, 20 mg photocatalysts, 1 wt% Pt, and the irradiation wavelength λ > 420 nm).

pristine CN. It is also worth noting that our results, including H_2 production rate and also AQY, are outstanding comparing with the most recent reports as listed in the Table. S2. As a comparison, the sample CN-TH which has a reverse operation sequence of protonation and thermal oxidation treatment, only has 7.3 times improvement compared to pristine CN. Furthermore, the photocatalytic stability of CN-HT was investigated over 15 h with 5 successive cycles, shown in the Fig. 1d. The results are displayed in the Fig. 1c. No notable decrease of the H_2 amount is observed in each cycle, indicative of the good stability of the sample of CN-HT in our experimental condition.

As a further study, H_2SO_4 and HNO_3 were selected to protonate the CN with followed thermal oxidation to prove the general effect of inorganic acids on promoting the performance of CN. As shown in the Fig. S2, the three samples demonstrate the H_2 evolution rates in the order of H_2SO_4 > HCl > HNO_3, with HER ability of 3.08, 2.24, and 1.76 mmol $h^{-1} g^{-1}$, respectively. Comparing to the pristine CN, all of them have an obvious improvement. It indicates that this method is a possible general approach to tune the properties of graphite-like layered materials. Although H_2SO_4 protonated CN has the best performance, the following discussion will still be concentrated on the HCl treated samples, considered that Cl ions will exert less effect on the final structure of CN as will be revealed in our following results.

3.2. Structure characterizations

In order to reveal the factors contributing to the dramatic enhancement in HER performance, the structure evolution of graphitic carbon nitrides under different treatments was investigated firstly by the X-ray diffraction patterns, as shown in the Fig. 2a. In these patterns, two typical diffraction peaks centered around 13.0° (100) and 27.6° (002) can be associated with the hydrogen bonds for maintaining an intralayer long-range atomic order and Van der Waals forces for controlling interlayer periodic stacking along the c-axis in graphitic carbon nitride, respectively [6,31]. Obviously, all the samples have the same structure. However, a slightly decreased intensity of (002) for the post treated samples indicate that protonation and calcination process can partially exfoliate the compact bulk CN into the fewer layer or porous CN. In detail, in a slightly acidic conditions, due to the existence of

plenty of (-C−N-) motifs in the framework, CN can be easily protonated by concentrated hydrochloric acid [23], thus resulting in the preliminary delamination of the protonated of CN [21]. Regarding the calcination process, the thermal etching effect of oxygen usually causes the corroded surface structure of CN, thus, leading to more irregular porous structures [32]. Wherein, the combination of first protonation and second calcination treatment, CN−HT, produces the fewer layer structure effectively due to the pre-delamination effect of acid and the further delamination effect of heat, respectively. On the other hand, positive peak shifts were only observed for the samples experienced thermal treating, CN−T and CN−HT, indicating the shortened distance between interlayers due to the introduced O species [32]. Our results also exclude the possible intercalation of Cl^- into the carbon nitrides layers, considering that the intercalation of Cl^- can arise the increase of interlayer distance [14]. The introducing of Cl^- will be further ruled out by the following FTIR and XPS results. Therefore, in the soaking process of CN in the HCl solution, only protons are introduced into its structures.

The introduced protons in the structure or the surface of graphitic carbon nitrides can be clearly proved by the Zeta potential experiment. Generally, the surface of CN powder without any modification in the aqueous solution is always negatively charged [28,33]. In this work, as shown in the Fig. 2b, pristine graphitic carbon nitrides also shows an average Zeta potential of -14.96 mV. While it changes to be 12.60 mV after protonation, implying its surface to be positively charged by the attacking of H^+ owing to the presence of abundant -C–N- motifs in the framework [27]. Interestingly, after the subsequent thermal oxidation treatment, its surface changes to be negative again, meaning the re-loss of the introduced protons in the thermal treatment, which may be consumed by forming an evolved gas, such as NH_3, in the thermal oxidation process.

Further, as shown by the TEM images in the Fig. 2c–f, all the post treated samples retain layered structure similarly to pristine CN. Wherein, the smooth surface without pores, which can be observed by naked eyes, is recorded for the sample CN and CN-H, indicative of the weak etching effect of protons on CN to create pores. However, only a lot of pits appear on the surface of CN-T. The absence of holes penetrating the matrix of CN reveals the stronger influence of thermal
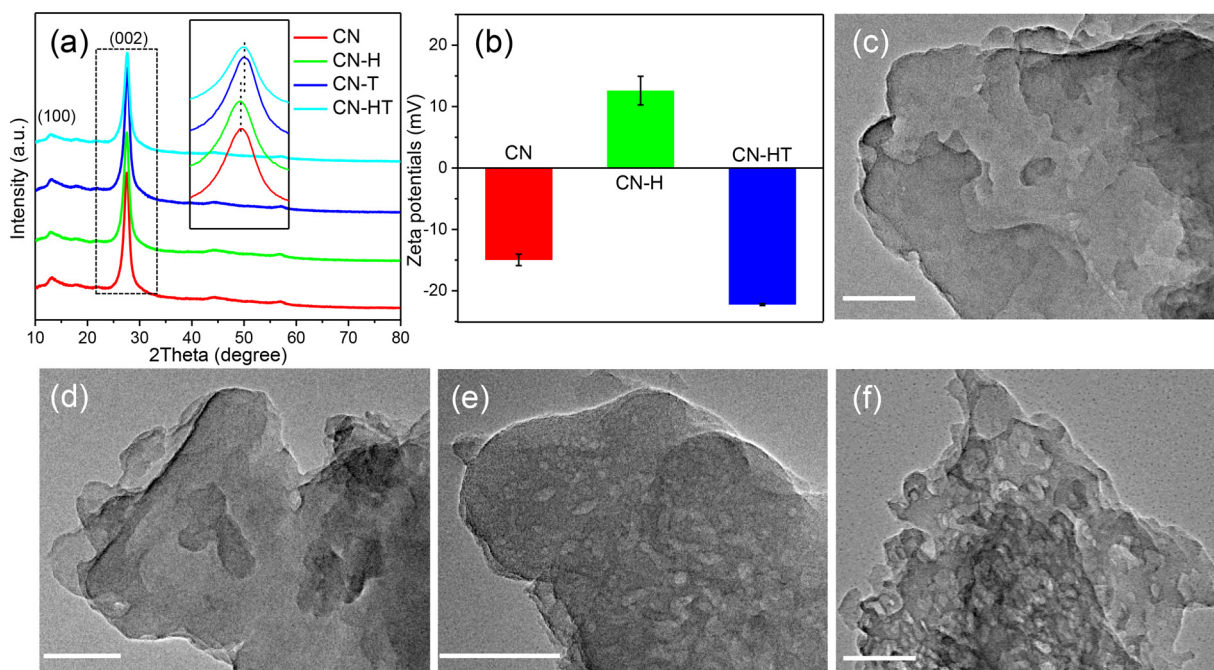

Fig. 2. (a) The XRD patterns of CN, CN-H, CN-T, and CN-HT; (b) The Zeta potentials of CN, CN-H, and CN-HT; TEM images of (c) CN, (d) CN-H, (e) CN-T, and (f) CN-HT. The scale bar in each TEM image is 100 nm.
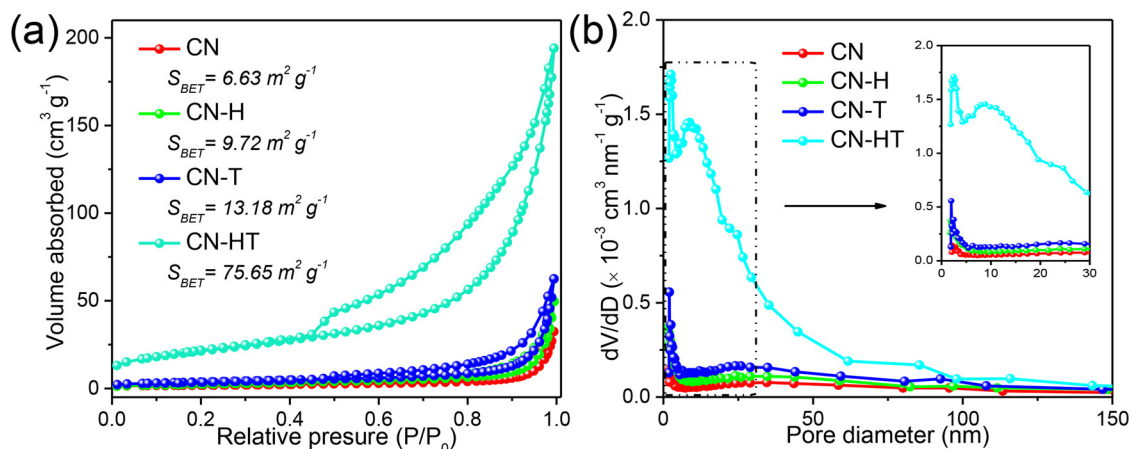
Fig. 3. (a) The N$_2$ adsorption-desorption isotherms and BET surface area and (b) pore size distribution curves of CN, CN-H, CN-T, and CN-HT.

oxidation on generating pores than protonation action. As a comparison, the same thermal oxidation conditions acting on CN-H resulted in numerous pores in bulk CN. Obviously, the pre-protonation effect can lead to more intense oxidant etching effect.

The detailed information about these pores was further analyzed by the N$_2$ adsorption-desorption isotherms. As displayed in the Fig. 3, the surface area is measured to be ca. 6.63, 9.72, 13.18, and 75.65 m^2 g^{-1} for CN, CN-H, CN-T, and CN-HT, respectively. The slight increase of BET area for the CN-H decodes the protonation effect on the imperfect polymer-like structure, resulting in its weak cleavage of both sheets and stacks [21]. Meanwhile, a more obvious increase of surface area for CN-T arises from the more intense oxidation etching effect under high temperature in the air [32]. Without any doubt, the largest surface area is detected for CN-HT due to the most significant influence of combined action of protonation and thermal oxidation on creating porous structures. On the other hand, based on the N$_2$ adsorption-desorption isotherms, a type IV with H3 hysteresis loop is detected for the CN-HT, indicating the porous structure with the pore size falling in the range of 1.6 nm to 100 nm. It further proves the pores rich structure for CN-HT. Generally, the porous structures of graphitic carbon nitride could offer abundant edges as active sites and channels for mass transfer during photocatalytic reactions and lead to a better performance [11]. It is worth noting here that the enhanced surface area of CN-HT is about 11.5 times higher than that of pristine CN, while the promoted HER activity is about 29.5 times higher. Consequently, the enhanced area is considered to be not the unique factor responsible for the improved hydrogen evolution performance. The modified physical and chemical properties may play important role as well.

The possible change of compositions and chemical states of modified CN were investigated by the FTIR and XPS spectra as shown in the Fig. 4. Evidently, from the FTIR spectra in Fig. 4a, all the band signals assigned to a typical graphitic carbon nitride can be observed for every sample, indicating their unchanged general chemical structures. In detail, the sharp peak around 806 cm^{-1} originates from the breathing mode of triazine ring [34,35]. As further showed by the enlarged view in Fig. S3, the thermal etched samples (CN−T and CN−HT) are shifted to 809 cm^{-1}, confirming the relatively lower amount of hydrogen bonds [10]. Here the abundant pores within the layer are supposed to decrease the probability of the formation of H bonds between H atoms with other atoms. The signals from 1800 to 1000 cm^{-1} are the typical stretching vibration modes of C=N and C−N heterocycles [34]. And the broad peaks between 3000 and 3600 cm^{-1} are contributed to N-H$_x$ stretching [19]. Consequently, the unchanged FTIR signals indicate that the CN after treating retains the polymeric melon units in the long-range atomic order patterns, consistent with other reported researches [21,23], excepting for a slightly eliminating of H bonds. In addition, no signals corresponding to the Cl- spectra can be detected which further

excludes the possible introduction on Cl in the acid soaking process. The conclusion is also supported by the full surveys of XPS and high resolution Cl 2p spectra as shown in the Fig. S4. Moreover, the full XPS survey indicated that all the samples contain only the element C, N, and O.

Further, the high resolution of C 1 s spectra is deconvolved into three components, as displayed in the Fig. 4b. For the pristine CN, the peak around 288.2 eV, 286.0 eV, and 284.8 eV are corresponding to the typical aromatic C–N = C coordination, C–NH$_x$ on the edges of hepta-zine units and adventitious hydrocarbons, respectively [22,36,37]. Wherein, the signals of catalyst CN−H have a slight chemical shift comparing to other three samples, implying the protonation resulting in changed local arrangement of C atoms after introducing protons [38]. On the other hand, the N1 s high resolution spectra of CN, shown in Fig. 4c, consisting of four peaks centered at 398.7 eV, 400.1 eV, 401.3 eV, and 404.4 eV, corresponding to the binding states of two-coordinated (N2c) state C–N–C, three coordinated (N3c) state N(C)3 in the heptazine units, C–N–H, and the charging effects, respectively [39,40]. It is worth noting that the binding ratios of the samples are quite different, originating from selective breaking of bonds in different treatments. In detail, the value of N2c/N3c is calculated to be 3.11 for pristine CN, while the theoretical value for N2c/N3c should be 3.00. The positive deviation of this value may come from its incomplete polymerization. However, this ratio becomes 0.96 and 1.31 for CN−H and CN−T, respectively, indicating the cleavage of N2c and destroy of C–NH in protonation or thermal etching processes. It further decreases to 0.56 for CN−HT. The loss of N2c inevitably breaks the framework of heptazine, which can be supported by the results of porous structures.

In the O 1 s high resolution spectra of CN, CN−T, and CN−HT in Fig. 4e, two peaks centered at 531.8 and 533.2 eV were observed. They can be attributed to C−OH and C−O−C species, respectively [41]. While in the CN−H, the signals of C−O−C and C−OH can be eliminated. It indicates that protons in the acid solution can effectively attack the O contained species. While the following thermal oxidation process brought the C−O−C and C−OH species into CN framework again. Additionally, the component of C−OH in CN-HT is much higher than that of CN and CN−T. The increased concentration of C−OH may induce a strengthened interaction with H$_2$O in the photocatalytic reaction process [42]. As proved by the surface hydrophilicity measurements shown in the Fig. 4f, after the successive treatment of protonation and thermal oxidation, the contact angle of CN-HT decreases to 46°, compared to 59° of pristine CN. It indicates a more hydrophilic surface, which will improve water adsorption and subsequent proton reduction [41].

Additionally, the elemental analysis was conducted to investigate the atom ratios change of all catalysts, and corresponding C/N and C/H values are listed in the Table. S3. Compared to previous reports [11,38], both of above ratios in all treated samples almost kept consistent with
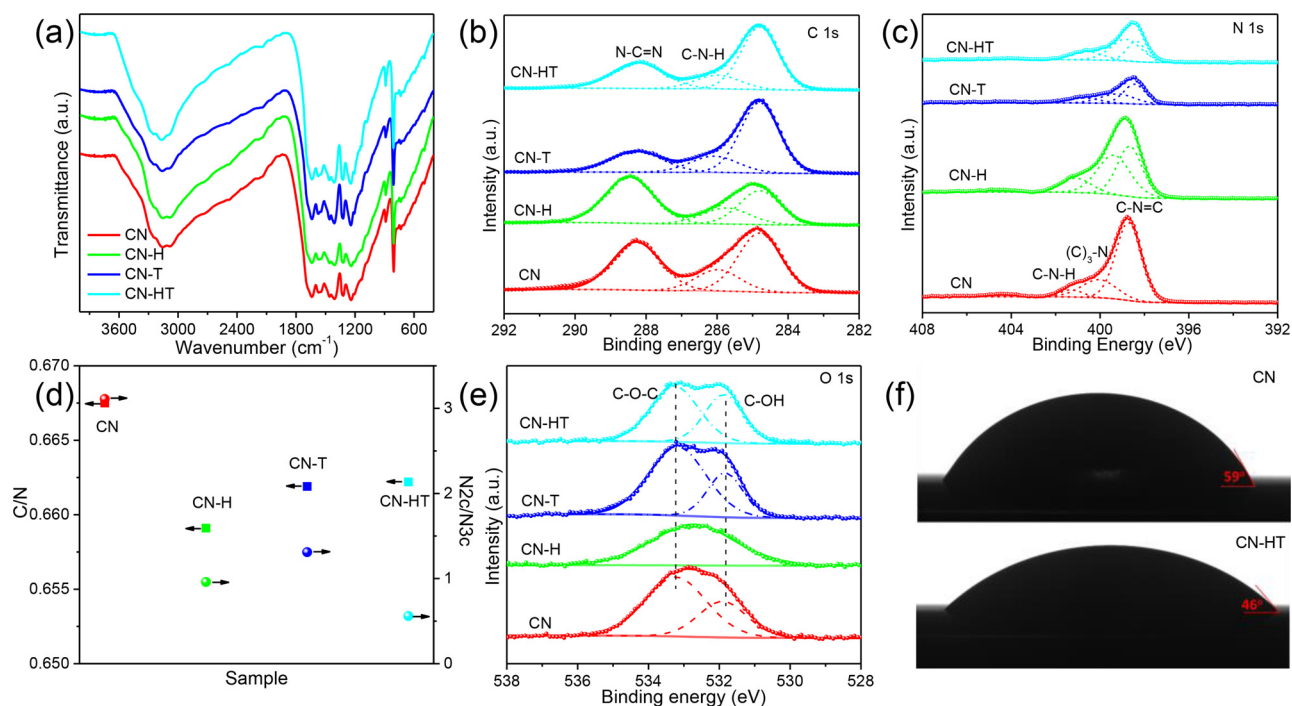
Fig. 4. (a) The FTIR spectra, (b) high resolution XPS spectra of C 1 s, (c) N 1 s, (d) the atomic ratio of C/N and N2c/N3c, (e) O 1 s, and of CN, CN-H, CN-T, and CN-HT; (f) The contact angle measurements of CN and CN-HT water suspension on the silicon plate.
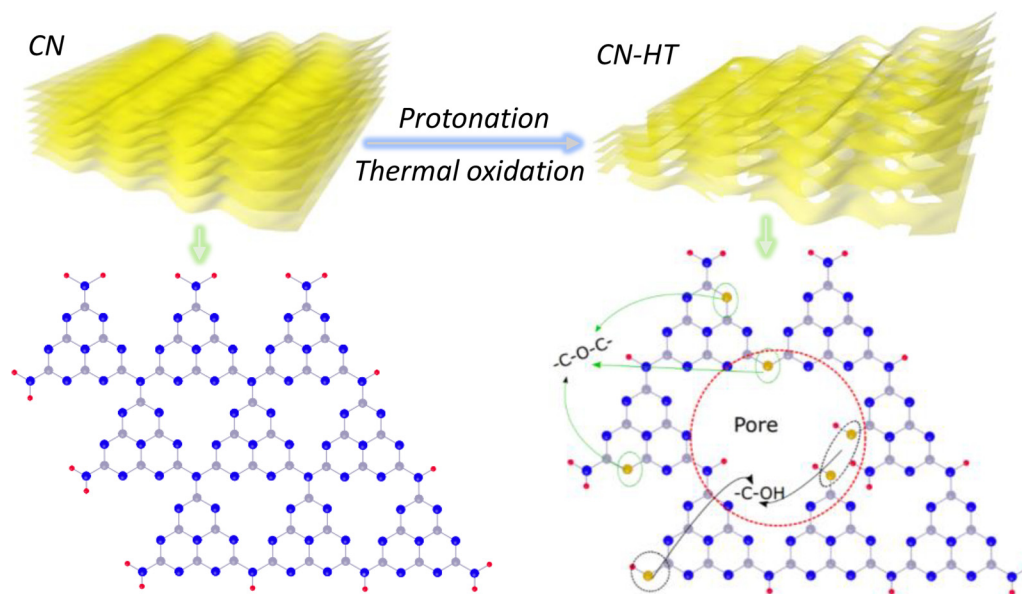

Fig. 5. The proposed structure diagram of CN and CN-HT. The balls in grey, blue, yellow, and red colors represent the C, N, O, and H atoms, respectively (For interpretation of the references to colour in this figure legend, the reader is referred to the web version of this article).

that of pristine CN, indicating the retained typical melon structures with numerous pores after the protonation and thermal oxidation processes. As a result, according to aforementioned analysis, the structures of pristine CN and CN-HT are shown in the Fig. 5.

3.3. Photo physical and chemical properties

The photo-physics and photo-chemistry properties of above samples were systematically investigated by the UV–vis diffraction reflectance spectra, steady-state PL spectra, electron paramagnetic resonance (EPR) spectra, and transient photocurrent response. According to the UV–vis spectra in the Fig. 6a, compared to pristine CN, no obvious light

absorption change is observed for the sample CN−H. It indicates that protonation have insignificant influence on optical absorption properties. The slight change can be attributed to the weak etching effect of acid. While regarding the sample CN−T and CN−HT, calcination treatment in the air effectively shifts its absorption edge to the more negative position. It could be due to the partial exfoliation and generation of porous structure for the bulky CN, which is consistent with the optical properties of CN obtained by other researchers [19,26,43]. The blue shift of absorption edge indicates the well-known quantum confinement effect by shifting the conduction and valence band edges in opposite directions [19,44]. Simultaneously, the enhanced absorption in the visible light region occurs to CN−HT, which may result from
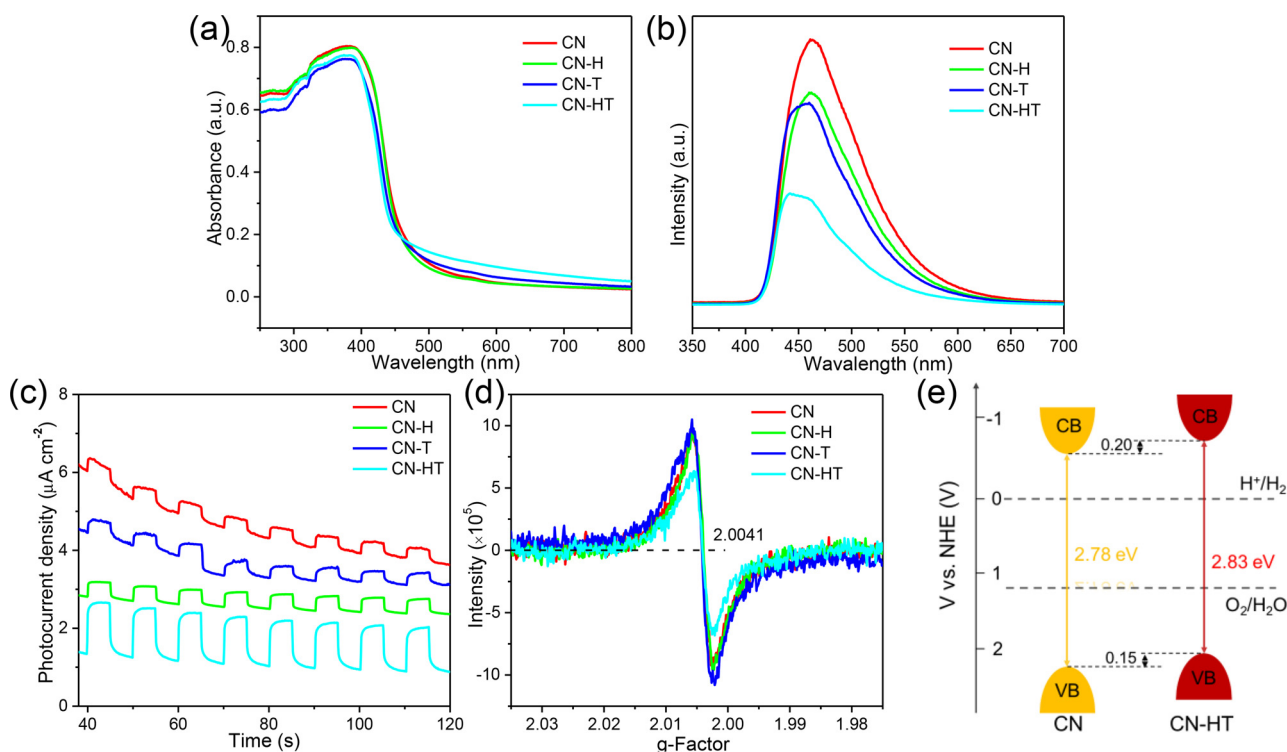
Fig. 6. The (a) UV–vis DRS, (b) PL, (c) transient photocurrent response, and (d) EPR spectra of CN, CN−H, CN−T, and CN−HT; (e) The band structure of CN and. CN−HT.

the slow effect of porous architecture on photons.

The recombination property of photo-induced charge carriers of all photocatalysts was detected by the steady-state PL spectra. As shown in the Fig. 6b, evidently, the change of fluorescence emission wavelength of each sample is consistent with that of absorption edge wavelength. All the post treated samples showed a quenched fluorescence emission intensity, meaning the lower radiative recombination of photoexcited electrons and holes. Wherein the lowest one is CN–HT, meaning its strongest separation and transfer efficiency of the photo induced charge carriers. Additionally, the further information about the transport behaviors of the photo generated charge carriers has been investigated by transient photocurrent response. As shown in the Fig. 6c, the largest photocurrent, undoubtedly, of CN–HT again prove its highest separation efficiency of photo-generated charge carriers.

The electron paramagnetic resonance (EPR) experiments were carried out to obtain more information on possible structural defects in different types of carbon nitride at room temperature. As shown in the Fig. 6d, all the samples exhibit a single Lorentzian line with a g value equivalent to 2.0041, which can be assigned to lone pair electrons in sp^2-carbon in the aromatic rings [13]. The signal intensity of CN–HT is much lower than that of pristine CN and also other samples. This indicates a decreased unpaired electron density due to the lower surface defect density [45,46], few-layer crystal structure [47], and a higher degree of polymerization [10]. Combining the results of CN–H, CN–T, and CN–HT, it can be found that the sequential operation of protonation and thermal oxidation on CN effectively decrease its surface defect density, which in turn facilitates photo induced charge carriers' separation and migration.

The band structure of CN and CN−HT was deduced from their KM functioned UV–vis spectra and the measurements of density of states (DOS) of the valence band by valence band XPS. As shown in the Fig. S5a, the band gap of CN and CN−HT is 2.78 eV and 2.83 eV, respectively, indicating the enlarged band gap of CN−HT. On the other hand, from Fig. S5b, negative VBM shift is observed for CN−HT caused by the successive protonation and thermal etching process. Accordingly, the

detailed band energy structure is illustrated in the Fig. 6e. Thereinto, compared to pristine CN, CN−HT has a more negative potential for CBM, representing the stronger driving force for reduction reaction of the excited electrons, resulting in the boosted photocatalytic H₂ evolution performance.

3.4. Mechanism for the enhanced photocatalytic activity

Based on above analysis, the possible reaction mechanism about the significant enhanced photocatalytic HER evolution of CN−HT was proposed. According to the typical microscopic reaction process on a photocatalyst particle [1], photons absorption is not obliged to the enhanced photocatalytic performance due to the blue shift of absorption edge for CN−HT. Regarding photo-induced charge carriers separation and migration efficiency, the porous structure of CN−HT owns larger surface area with the abundant lateral edges/surfaces of the pore walls provides additional reductive reaction sites and as well as shortens the diffusion lengths of photoexcited electrons and holes from bulk to surface. Meanwhile, the porous structure also contributes to the mass diffusion of reactants molecular. While the promoted surface area is not the unique contribution for the enhanced H₂ evolution performance. The decreased defect density also play an important role in carriers transportation process. Regarding to the photocatalytic redox reactions on the surface, up-shift conduction band minimum possesses stronger reduction ability to reduce protons to H₂. Furthermore, the re-introduced C−OH species in CN−HT, more abundant than that of other samples, fortify its interaction with environmental redox species which, in turn, is expected to facilitate the catalytic performance. As a consequence of these favorable changes in improving all the last two basic processes of photocatalysis, the carbon nitride subjected to successive protonation and thermal etching processes results in a significantly enhanced photocatalytic hydrogen generation activity under visible light. Furthermore, the difference in H₂ production performance for CN−HT protonated by HCl, H₂SO₄, and HNO₃ may originate from their different charge separation and transportation properties, as shown in

the Fig. S6a and b.

4. Conclusions

In summary, we have developed a facile method to prepare porous structure graphitic carbon nitride with a high product yield and an outstanding photocatalytic activity. In preparing process, we discovered the important role of treatment sequence on the final performance. The g-C$_3$N$_4$ subjected to firstly acid protonation and secondly heat etching exhibited almost 29.5 times higher H$_2$ evolution rate compared to the untreated g-C$_3$N$_4$. While the sample CN-TH subjecting to a reverse operation sequence of protonation and thermal oxidation treatment only has 7.3 times improvement compared to pristine CN. The significantly enhanced activity originated from the strengthened charge carrier separation, promoted water reduction ability, and porous structure, which could provide more reaction sites and benefit from the transportation of reactant molecules. The results achieved in this study may also provide a new facile approach for tailoring the microstructure of layered materials to achieve improved performance not only for the application of photocatalysis, but also in many other fields

Acknowledgements

Appendix A. Supplementary data

Supplementary material related to this article can be found, in the online version, at doi:https://doi.org/10.1016/j.apcatb.2018.07.039.

References

[1] X. Chen, S. Shen, L. Guo, S.S. Mao, Chem. Rev. 110 (2010) 6503–6570.
[2] A. Kudo, Y. Miseki, Chem. Soc. Rev. 38 (2009) 253–278.
[3] W.-J. Ong, L.-L. Tan, Y.H. Ng, S.-T. Yong, S.-P. Chai, Chem. Rev. 116 (2016) 7159–7329.
[4] S. Sun, S. Liang, Nanoscale 9 (2017) 10544–10578.
[5] D. Masih, Y. Ma, S. Rohani, Appl. Catal. B 206 (2017) 556–588.
[6] Y. Kang, Y. Yang, L.C. Yin, X. Kang, L. Wang, G. Liu, H.M. Cheng, Adv. Mater. 28 (2016) 6471.
[7] Y. Zeng, C. Liu, L. Wang, S. Zhang, Y. Ding, Y. Xu, Y. Liu, S. Luo, J. Mater. Chem. A 4 (2016) 19003–19010.
[8] Y. Hong, C. Li, Z. Fang, B. Luo, W. Shi, Carbon 121 (2017) 463–471.
[9] Y. Guo, J. Li, Y. Yuan, L. Li, M. Zhang, C. Zhou, Z. Lin, Angew. Chem. Int. Ed. 55 (2016) 14693–14697.
[10] H. Lan, L. Li, X. An, F. Liu, C. Chen, H. Liu, J. Qu, Appl. Catal. B 204 (2017) 49–57.
[11] W. Tu, Y. Xu, J. Wang, B. Zhang, T. Zhou, S. Yin, S. Wu, C. Li, Y. Huang, Y. Zhou, ACS Sustain. Chem. Eng. 5 (2017).
[12] J. Li, W. Cui, Y. Sun, Y. Chu, W. Cen, F. Dong, J. Mater. Chem. A 5 (2017) 9358–9364.
[13] G. Zhang, M. Zhang, X. Ye, X. Qiu, S. Lin, X. Wang, Adv. Mater. 26 (2014) 805–809.
[14] C. Liu, Y. Zhang, F. Dong, A.H. Reshak, L. Ye, N. Pinna, C. Zeng, T. Zhang, H. Huang, Appl. Catal. B 203 (2017) 465–474.
[15] X. She, J. Wu, H. Xu, Z. Mo, J. Lian, Y. Song, L. Liu, D. Du, H. Li, Appl. Catal. B 202 (2017) 112–117.
[16] D. Zheng, X.N. Cao, X. Wang, Angew. Chem. Int. Ed. 55 (2016) 11512–11516.
[17] M. Wang, P. Ju, J. Li, Y. Zhao, X. Han, Z. Hao, ACS Sustain. Chem. Eng. 5 (2017) 7878–7886.
[18] Q. Tay, P. Kanhere, C.F. Ng, S. Chen, S. Chakraborty, A.C.H. Huan, T.C. Sum, R. Ahuja, Z. Chen, Chem. Mater. 27 (2015) 4930–4933.
[19] P. Niu, L. Zhang, G. Liu, H.M. Cheng, Adv. Funct. Mater. 22 (2012) 4763–4770.
[20] Y. Li, R. Jin, Y. Xing, J. Li, S. Song, X. Liu, M. Li, R. Jin, Adv. Energy Mater. 6 (2016).
[21] Y. Zhang, A. Thomas, M. Antonietti, X. Wang, J. Am. Chem. Soc. 131 (2009) 50.
[22] Z. Zhou, Y. Shen, Y. Li, A. Liu, S. Liu, Y. Zhang, Acs Nano 9 (2015) 12480.
[23] T.Y. Ma, Y. Tang, S. Dai, S.Z. Qiao, Small 10 (2014) 2382.
[24] O. Fontelles-Carceller, M.J. Muñoz-Batista, M. Fernández-García, A. Kubacka, ACS Appl. Mater. Interfaces 8 (2016) 2617–2627.
[25] H. Wang, X. Yuan, Y. Wu, G. Zeng, X. Chen, L. Leng, H. Li, Appl. Catal., B 174 (2015) 445–454.
[26] J. Xu, L. Zhang, R. Shi, Y. Zhu, J. Mater. Chem. A 1 (2013) 14766–14772.
[27] W.-J. Ong, L.-L. Tan, S.-P. Chai, S.-T. Yong, A.R. Mohamed, Nano Energy 13 (2015) 757–770.
[28] X. Yang, F. Qian, G. Zou, M. Li, J. Lu, Y. Li, M. Bao, Appl. Catal. B 193 (2016) 22–35.
[29] S. Kang, L. Zhang, C. Yin, Y. Li, L. Cui, Y. Wang, Appl. Catal. B 211 (2017) 266–274.
[30] B. Luo, R. Song, D. Jing, Chem. Eng. J. 332 (2017) 499–507.
[31] F. Fina, S.K. Callear, G.M. Carins, J.T.S. Irvine, Chem. Mater. 27 (2015) 2612–2618.
[32] L. Yang, J. Huang, L. Shi, L. Cao, Q. Yu, Y. Jie, J. Fei, H. Ouyang, J. Ye, Appl. Catal. B 204 (2017) 335–345.
[33] L. Ma, H. Fan, K. Fu, S. Lei, Q. Hu, H. Huang, G. He, ACS Sustain. Chem. Eng. 5 (2017) 7093–7103.
[34] X. She, J. Wu, J. Zhong, H. Xu, Y. Yang, R. Vajtai, J. Lou, Y. Liu, D. Du, H. Li, Nano Energy 27 (2016) 138–146.
[35] Q. Xiang, J. Yu, M. Jaroniec, J. Phys. Chem. C 115 (2011) 7355–7363.
[36] C. Dong, Z. Ma, R. Qie, X. Guo, C. Li, R. Wang, Y. Shi, B. Dai, X. Jia, Appl. Catal. B (2017).
[37] H. Yu, R. Shi, Y. Zhao, T. Bian, Y. Zhao, C. Zhou, G.I. Waterhouse, L.Z. Wu, C.H. Tung, T. Zhang, Adv. Mater. 29 (2017) 1605148.
[38] P. Niu, M. Qiao, Y. Li, L. Huang, T. Zhai, Nano Energy 44 (2018) 73–81.
[39] P. Yang, H. Ou, Y. Fang, X. Wang, Angew. Chem. Int. Ed. 129 (2017) 4050–4054.
[40] D.J. Martin, K. Qiu, S.A. Shevlin, A.D. Handoko, X. Chen, Z. Guo, J. Tang, Angew. Chem. Int. Ed. 53 (2014) 9240–9245.
[41] Y. Wang, M.K. Bayazit, S.J. Moniz, Q. Ruan, C.C. Lau, N. Martsinovich, J. Tang, Energy Environ. Sci. 10 (2017) 1643–1651.
[42] X.L. Wang, W.Q. Fang, H.F. Wang, H. Zhang, H. Zhao, Y. Yao, H.G. Yang, J. Mater. Chem. A 1 (2013) 14089–14096.
[43] X. She, L. Liang, H. Ji, M. Zhao, Y. Li, L. Huang, D. Du, X. Hui, H. Li, Appl. Catal. B 187 (2016) 144–153.
[44] A.P. Alivisatos, Science (80-) 271 (1996) 933–937.
[45] G. Zhang, J. Zhang, M. Zhang, X. Wang, J. Mater. Chem. 22 (2012) 8083–8091.
[46] P. Qiu, C. Xu, H. Chen, F. Jiang, X. Wang, R. Lu, X. Zhang, Appl. Catal. B 206 (2017) 319–327.
[47] H. Ou, L. Lin, Y. Zheng, P. Yang, Y. Fang, X. Wang, Adv. Mater. 29 (2017) 1700008.